Efficient Dynamical Field-Theoretic Simulations for Multi-Component Systems

Timothy Quah,[1] Christopher Balzer,[2] Kris T. Delaney,[2] and Glenn H. Fredrickson[1, 2, 3]

[1)] *Department of Chemical Engineering, University of California, Santa Barbara, California 93106, USA*

[2)] *Materials Research Laboratory, University of California, Santa Barbara, California 93106, USA*

[3)] *Materials Department, University of California, Santa Barbara, California 93106, USA*

(*Electronic mail: ghf@ucsb.edu)

(Dated: 28 February 2025)

Understanding the phase behavior and dynamics of multi-component polymeric systems is essential for designing materials used in applications ranging from biopharmaceuticals to consumer products. While computational tools for understanding the equilibrium properties of such systems are relatively mature, simulation platforms for investigating non-equilibrium behavior are comparatively less developed. Dynamic self-consistent field theory (DSCFT) is a method that retains essential microscopic thermodynamics while enabling a continuum-level understanding of multi-component, multi-phase diffusive transport. A challenge with DSCFT is its high computational complexity and cost, along with the difficulty of incorporating thermal fluctuations. External potential dynamics (EPD) offers a more efficient approach to studying inhomogeneous polymers out of equilibrium, providing similar accuracy to DSCFT but with significantly lower computational cost. In this work, we introduce an extension of EPD to enable efficient and stable simulations of multi-species, multi-component polymer systems, while embedding thermodynamically consistent noise. We validate this framework through simulations of a triblock copolymer melt and spinodally decomposing binary and ternary polymer blends, demonstrating its capability to capture key features of phase separation and domain growth. Furthermore, we highlight the role of thermal fluctuations in early-stage coarsening. This study provides new insights into the interplay between stochastic and deterministic effects in the dynamic evolution of polymeric fluids with the EPD framework offering a robust and scalable approach for investigating the complex dynamics of multi-component polymeric materials.

I. INTRODUCTION

Polymeric formulations are essential in a wide range of applications, such as elastomers, paints, adhesives, personal care products, pharmaceuticals, and plastic products.[1–5] A key challenge in designing multi-component formulations is understanding miscibility, as even small chemical differences between components can lead to structural heterogeneity.[6] The length scale of the structural heterogeneity can significantly alter a range of material properties, including mechanical,[7,8] rheological,[9–11] transport,[12–14] and optical or photonic properties.[15–17] Another major challenge in formulation development is the high dimensionality of the parameter space, which may include composition, chemistry, and chain topology, among other factors.[18] Due to material and time constraints, relying solely on experimental techniques to navigate the parameter space is unfeasible. Therefore, theoretical and computational tools are indispensible for gaining insights and establishing design principles in order to obtain formulations with tailored properties.[19,20]

Theoretical tools for predicting polymer formulation properties must capture continuum-level phenomena while also retaining essential microscopic details, such as chain connectivity.[21,22] Among such methods, molecularly derived polymer field theories are particularly effective for probing the equilibrium properties of multicomponent polymer formulations.[20,23] The most common treatment of polymer field theory is self-consistent field theory (SCFT), which has successfully elucidated the self-assembly behavior of a wide variety of polymeric systems.[20,24–27] SCFT is quantitatively predictive when thermal fluctuations are weak and well ordered equilibrium states are achieved. However, when thermal fluctuations are strong or the system is near a critical phase transition, field-theoretic simulations (FTS) become necessary, allowing for the study of fluctuation-driven phenomena.[23] In reality, materials often do not reach well ordered equilibrium states within experimental time scales, making an understanding of the material's processing history critical – an aspect that both SCFT and FTS do not attempt to address .[28]

Dynamic variants of equilibrium field theories have been developed to study kinetic pathways toward equilibrium states. The most common among these is dynamic self-consistent field theory (DSCFT).[28–32] DSCFT utilizes a density-explicit field theory framework that retains both mesoscopic density fields and auxiliary species fields. Density fields evolve according to Model B conserved dynamics,[33] while the auxiliary species fields are solved self-consistently on each timestep.[20,28] DSCFT has been effectively used to study the self-assembly behavior of block copolymers in both solutions and melts[29,30,34,35], during solvent evaporation[36,37], in systems under shear[38], and in systems where hydrodynamic interactions are significant[39,40]. However, DSCFT suffers from significant computational cost as SCFT relaxation steps must be performed at each time step to compute thermodynamic forces.

A significant, and often overlooked, challenge with DSCFT is the inclusion of thermal fluctuations. While the theoretical framework can be extended to account for these corrections, numerical simulations incorporating them are scarce.[30,34,41] Stochastic DSCFT typically suffers from numerical instability, arising from the failure to maintain positive solutions when integrating the mesoscopic density fields. Previous FTS work with the density-explicit field theory showed that preserving positive solutions requires numerical schemes with strong accuracy or the ability to accurately track stochastic trajectories.[42] However, constructing such strong order schemes for correlated noise is non-trivial. In the density-explicit formalism, the failure to prevent negative densities can be catastrophic, resulting in numerical pathologies including exploding trajectories, overflow/underflow, and/or negative densities that persist throughout the simulation. In contrast, the auxiliary field (AF) formalism, which relies solely on auxiliary fields with an exponential-like relationship to mesoscopic density fields, allows for transient negative density values without causing catastrophic numerical issues. Consequently, AF dynamical models are generally more tolerant to fluctuations.[43,44]

Obtaining an AF dynamical model requires rewriting the dynamical equations using auxiliary fields, typically termed the external potential dynamics (EPD) method.[45] Since EPD directly evolves the auxiliary field, the method in principle does not require SCFT iteration loops to be performed at each time step. As a consequence of the gain in computational efficiency, EPD has been effectively applied to investigate the nonequilibrium behavior of polymers and block copolymers in both solutions and melts[34,43–49], under the influence of electric and magnetic fields[50,51], and in systems with hydrodynamic interactions[52]. However, EPD has not yet been generalized beyond two species or components to the multi-species exchange model, which would enable its application to broader classes of formulated polymer systems.[53] Moreover, the literature on EPD that includes thermal fluctuations is very limited, in spite of this being one of the main reasons for pursuing EPD over DSCFT.[43,44]

In this work, we address both issues by developing an EPD method based on the multi-species exchange model and examining the impact of incorporating thermal fluctuations in EPD. Sec. II introduces the models and numerical schemes used, and Sec. III presents exemplary results from three model systems: a triblock copolymer melt, a binary polymer blend, and a ternary polymer blend.

II. THEORETICAL AND NUMERICAL METHODS

This work aims to extend EPD to accommodate arbitrary numbers of species and components by generalizing it to a multi-species exchange model. Since the dynamical models incorporate molecularly derived thermodynamic forces, we first introduce the equilibrium basis for these forces, generalized to include any number of species and components. We subsequently present the dynamical models that we develop and investigate in detail.

A. Equilibrium Models

As a starting point, we outline the density-explicit auxiliary field framework used in both equilibrium self-consistent field theory (SCFT) and dynamic self-consistent field theory (DSCFT). The following field theory describes the thermodynamic behavior of multi-component polymeric formulations within the canonical ensemble. Our formalism retains both mesoscopic density fields ϕ_j and auxiliary species fields ψ_j, where j is an index that runs from 1 to the number of monomer species S.[20,42] The model embeds non-bonded interactions through Flory-Huggins χ parameters and enforces the incompressibility constraint through a harmonic penalty, where ζ is the Helfand compressibility parameter with $\zeta \to \infty$ corresponding to an incompressible system.[53–55] In a canonical ensemble with fixed volume V, temperature T, and number of molecules n_p of each polymer component ($p \in (1,2,\ldots,P)$), with P the number of components, the partition function $Z_c(\{n\},V,T)$ is given by

$$\begin{aligned} Z_c(\{n\},V,T) &= Z_0 \prod_{j,k=1}^{S} \int D\psi_j \int D\phi_k \exp(-H[\{\phi\},\{\psi\}]) \quad (1) \\ H[\{\phi\},\{\psi\}] &= C\left[\frac{1}{2}\sum_{j,k=1}^{S}\chi_{jk}N\int d\mathbf{r}\,\phi_j(\mathbf{r})\phi_k(\mathbf{r}) + \frac{1}{2}\zeta N\int d\mathbf{r}\left(\sum_j \phi_j - 1\right)^2\right. \\ &\qquad \left. -i\sum_j\int d\mathbf{r}\,\phi_j(\mathbf{r})\psi_j(\mathbf{r}) - \bar{V}\sum_{p=1}^{P}\frac{\bar{\phi}_p}{\alpha_p}\ln Q_p[\{\psi\}]\right] \quad (2) \end{aligned}$$

Here Z_0 is the reference partition function of a non-interacting polymer mixture, and H is the effective Hamiltonian for the interacting system. Different monomer species interact via Flory-Huggins interactions parameterized by the matrix χ_{jk}, and the Helfand compressibility parameter ζ. Q_p

represents the single-chain partition function of chain component p, $\bar{\phi}_p$ is the average volume fraction of that component, and $\alpha_p = N_p/N$ is the relative chain length of that component relative to a reference chain length N. Spatial coordinates in the model have been non-dimensionalized using a reference radius of gyration, $R_g = b(N/6)^{1/2}$, with b a reference statistical segment length. The fields $\phi_j(\mathbf{r})$ represent dimensionless segment densities that are scaled by the total average segment density ρ_0. The species auxiliary fields $\psi_j(\mathbf{r})$ are scaled by a reference chain length N. $\bar{V} = V/R_g^3$ is the dimensionless volume, and $C = \rho_0 R_g^3 N^{-1}$ is a reference dimensionless chain concentration. When thermal fluctuations are included, C is the relevant Ginzburg parameter that regulates the strength of the fluctuations.

The single chain partition functions $Q_p[\{\psi\}]$ for continuous linear chains are evaluated by

$$Q_p = \frac{1}{V}\int d\mathbf{r}\, q_p(\mathbf{r}, \alpha_p; \{\psi\}) \tag{3}$$

where the propagators $q_p(\mathbf{r}, s)$ are obtained by integrating the modified diffusion equation along the contour position s

$$\frac{\partial q_p(\mathbf{r}, s)}{\partial s} = \left[\frac{b(s)^2}{b^2}\nabla^2 - \psi_p(\mathbf{r}, s)\right] q_p(\mathbf{r}, s) \tag{4}$$

where $b(s)$ is the statistical segment length of a monomer at contour position s. The solution of Eq. (4) is developed from an initial condition given by $q_p(\mathbf{r}, 0) = 1$. The auxiliary field $\psi_p(\mathbf{r}, s)$ is defined as $\psi_j(\mathbf{r})$ if the polymer segment at contour position s is of species type j.

An alternate representation of the same model can be obtained with the auxiliary-field framework (AF). In this framework, the model given in Eq. (2) is transformed by analytical evaluation of the ϕ_j field integrals.[53] To conduct these Gaussian integrals, an eigenvalue decomposition is applied, changing the character of the species auxiliary fields to pressure-like and exchange-like auxiliary fields. The resulting "multi-species exchange" representation of the partition function has the form

$$Z_c(n, V, T) = \prod_{j=1}^{S}\int D\mu_j \exp(-H[\{\mu\}]) \tag{5}$$

$$\begin{aligned} H[\{\mu\}] = C\Bigg[& -\sum_{j=1}^{S}\frac{(\zeta N)^{-1/2}}{2d_j}\int d\mathbf{r}\, \mu_j^2(\mathbf{r}) \\ & - \sum_{j,k=1}^{S}\frac{\mathrm{O}_{kj}}{d_j(\zeta N)^{-1/2}}\int d\mathbf{r}\, \mu_j(\mathbf{r}) - \bar{V}\sum_{p=1}^{P}\frac{\bar{\phi}_p}{\alpha_p}\ln Q_p[\{\psi\}]\Bigg] \end{aligned} \tag{6}$$

where we have omitted the non-interacting reference prefactor Z_0 and "normalizing denominator" factors in Z_c.[23,53] The normal mode fields $\mu_j(\mathbf{r})$ are linearly related to the species fields by an orthogonal transformation, with species-like fields given by $\underline{\psi} = \underline{\underline{O}} \cdot \underline{\mu}$. Here, d_j represents the jth eigenvalue of the $S \times S$ interaction matrix $(\zeta N)^{-1/2} \underline{\underline{\chi}} N + (\zeta N)^{1/2} \underline{\underline{1}}$, with $\underline{\underline{1}}$ the $S \times S$ matrix with all entries equal to 1, and $\underline{\underline{O}}$ is an orthogonal matrix formed from a direct product of the eigenvectors.

A normal mode field $\mu_j(\mathbf{r})$ is characterized as being "exchange-like" if its corresponding eigenvalue is negative ($d_j < 0$) and "pressure-like" if $d_j > 0$. The eigenmode with the largest positive eigenvalue is termed the "pressure" mode and denoted $\mu_+(\mathbf{r})$. All pressure-like modes have been Wick-rotated by a factor of $i = \sqrt{-1}$ in the multi-species exchange representation of Eqns. (5) & (6). This ensures that the saddle-point (mean-field) values of all fields are real.

With these two equilibrium model representations now outlined, we proceed to consider how they can be embeded in a dynamics scheme to investigate nonequilibrium phenomena in multi-component polymer systems.

B. Dynamic Models

In this work, we employ Model B dynamics to describe the time evolution of conserved density fields.[33] The governing equations preserve mass conservation, while connecting chemical potential gradients to diffusive fluxes, ensuring thermodynamic consistency. A stochastic noise term is further included to represent random thermal forces. A key assumption in Model B is that diffusive mass transport is dominant and convective transport, e.g. manifested as hydrodynamic interactions, can be neglected.

The mesoscopic density fields, ϕ_k, evolve in time according to:

$$\begin{aligned} \frac{\partial \phi_k(\mathbf{r})}{\partial \bar{t}} &= \sum_{l=1}^{S} \nabla \cdot \left(\mathrm{M}_{kl}(\mathbf{r}, \bar{t}; [\{\phi\}]) \nabla \frac{\delta F[\{\phi\}]}{\delta \phi_l(\mathbf{r}, \bar{t})} \right) + \eta_k(\mathbf{r}, \bar{t}) && (7) \\ \mathrm{M}_{kl}(\mathbf{r}, \bar{t}; [\{\phi\}]) &= \phi_k(\mathbf{r}, \bar{t}) \delta_{kl} && (8) \end{aligned}$$

where M_{kl} is the mobility matrix, and the mobility form follows the local-coupling approximation.[29] Time has been nondimensionalized as $\bar{t} = t/\tau$ where $\tau = R_g^2 C / D_{\mathrm{Rouse}}$ where D_{Rouse} is the Rouse self-diffusion coefficient of the reference polymer of length N.

The thermal fluctuation term, $\eta_k(\mathbf{r}, \bar{t})$, obeys the fluctuation-dissipation theorem, with the following moments:

$$\begin{aligned} \langle \eta_k(\mathbf{r}, \bar{t}) \rangle &= 0 && (9) \\ \langle \eta_l(\mathbf{r}, \bar{t}) \eta_k(\mathbf{r}', \bar{t}') \rangle &= -2 \nabla \cdot \left[\mathrm{M}_{kl}(\mathbf{r}, \bar{t}; [\{\phi\}]) \nabla \delta(\mathbf{r} - \mathbf{r}') \right] \delta(\bar{t} - \bar{t}') && (10) \end{aligned}$$

In practice, this noise term is numerically implemented using a previously reported algorithm, and further details regarding its construction and validation can be found in the Supplementary Information.[41]

The functional derivative $\delta F/\delta\phi_l$ in Eq. (7) can be viewed as the local chemical potential of segment species l and provides the thermodynamic driving force for multicomponent diffusion. This quantity is defined by:

$$\frac{\delta F[\{\phi\}]}{\delta\phi_j(\mathbf{r},t)} = \left\langle \frac{\delta H[\{\phi\},\{\psi\}]}{\delta\phi_j(\mathbf{r},t)} \right\rangle_{\{\psi\}} \tag{11}$$

where $\left\langle \frac{\delta H[\{\phi\},\{\psi\}]}{\delta\phi_j(\mathbf{r},t)} \right\rangle_{\{\psi\}}$ denotes an equilibrium average over the auxiliary $\{\psi\}$ fields with the $\{\phi\}$ fields constrained to their instantaneous values. Although this average can be computed without approximation by using complex-Langevin sampling, this would add very considerable computational cost, so it is typically approximated using the saddle-point/mean-field configuration for $\{\psi\}$. This $\{\psi\}$ saddle-point configuration must be computed at each time step as the constrained $\{\phi\}$ variables are updated. Typically, the computation involves an iterative procedure that is initialized from the saddle-point fields at the previous time step. Overall, this approach, known as dynamical self-consistent field theory (DSCFT), accurately preserves thermodynamic information but is computationally more expensive per time step (by a factor of order 10) than a field update in an equilibrium SCFT simulation.[23]

The approach we take in this work is to replace the mesoscopic density fields, $\{\phi\}$, with the exchange and pressure-like normal mode fields, $\{\mu\}$, in the multicomponent diffusion equations outlined above. This strategy is not new, but is a generalization of the external potential dynamics (EPD) method.[45] EPD relies on a chain rule to transform the equations of motion for the $\{\phi\}$ fields to corresponding equations for the time dependent evolution of the normal mode fields $\{\mu\}$. The corresponding dynamical equation is:

$$\frac{\partial\mu_j(\mathbf{r},\bar{t})}{\partial\bar{t}} = \sum_k \int d\mathbf{r}' \, \frac{\delta\mu_j(\mathbf{r},\bar{t})}{\delta\phi_k(\mathbf{r}',\bar{t})} \frac{\partial\phi_k(\mathbf{r}',\bar{t})}{\partial\bar{t}} \tag{12}$$

The typical way that the Jacobian $\delta\mu_j/\delta\phi_k$ is computed in ETD is to replace the mesoscopic density field ϕ_k with a linearized (RPA) approximation of the "conventional" equilibrium density field operator $\tilde{\phi}_k(\mathbf{r};[\{\mu\}])$,[43,45,47] which is both nonlocal and nonlinear in $\{\mu\}$. However, a more convenient "alternative" density field operator $\tilde{\phi}_{k,a}(\mathbf{r};[\{\mu\}])$ that is both linear and local in $\{\mu\}$ can be derived by a functional integration by parts.[20,23] By following this path, as detailed in the Supplementary Information, the inverse of the Jacobian can be expressed as

$$\frac{\delta\tilde{\phi}_{k,a}(\mathbf{r}';[\{\mu\}])}{\delta\mu_j(\mathbf{r})} = \frac{(\zeta N)^{-1/2}\,\mathrm{O}_{kj}}{d_j}\delta(\mathbf{r}-\mathbf{r}') \equiv N_{kj}\delta(\mathbf{r}-\mathbf{r}') \tag{13}$$

By combining these equations, the dynamic equation for μ becomes:

$$\begin{aligned}
\frac{\partial\mu_k(\mathbf{r},\bar{t})}{\partial\bar{t}} &= \gamma_k\sum_l^S \nabla\cdot\left(\mathrm{M}_{kl}(\mathbf{r},\bar{t};[\{\mu\}])\nabla\gamma_l\frac{\delta H[\{\mu\}]}{\delta\mu_l(\mathbf{r},\bar{t})}\right) + \gamma_k\eta_k(\mathbf{r},\bar{t}) \qquad (14)\\
\mathrm{M}_{kl}(\mathbf{r},\bar{t};[\{\mu\}]) &= \sum_m \mathrm{N}^{-1}_{km}\tilde{\phi}_m(\mathbf{r},\bar{t};[\{\mu\}])(\mathrm{N}^{-1})^T_{ml} \qquad (15)\\
\gamma_k &= \begin{cases} 1, & d_k < 0 \\ i=\sqrt{-1}, & d_k > 0 \end{cases} \qquad (16)
\end{aligned}$$

where the thermal noise term $\eta_k(\mathbf{r},\bar{t})$ follows the same statistics as previously described. The factors of γ_k are a consequence of the Wick rotation of the pressure and pressure-like fields. We have also chosen to approximate the mesoscopic density field by the conventional density operator $\tilde{\phi}_m$ in the mobility of Eq. (15), because it was found to produce more stable and physically realistic dynamics than that produced by the alternative density operator $\tilde{\phi}_{m,a}$.

The multi-species dynamical scheme of Eq. (14) can in principle be applied as written. However, we have found that a slight modification greatly improves numerical stability. Specifically, we isolate the pressure mode μ_+ with the largest positive eigenvalue d_+ from the other $S-1$ modes, denoted $\{\mu'\}$. The latter are updated with diffusive stochastic dynamics according to Eq. (14), but the pressure mode is deterministically relaxed at each time step to its partial saddle-point (PSP) configuration.[56] This approach forces the pressure field to respond instantaneously to the remaining fields and ensures a dynamical trajectory that does not allow large deviations from fluid incompressibility. Applying the PSP scheme involves approximating the integral over the pressure-like field, μ_+, using a saddle-point approximation. The saddle-point pressure field, $\mu_+^*(\mathbf{r},t;[\{\mu'\}]$, is determined by solving the following equation:

$$0 = \left.\frac{\delta H[\{\mu\}]}{\delta\mu_+(\mathbf{r},t)}\right|_{\mu_+^*} \tag{17}$$

at fixed/specified $\{\mu'\}$. Numerical solutions for this equation are obtained by an iterative procedure similar to that used in the saddle-point evaluation of Eq. (11).

C. Simulation Details

For all calculations involving EPD we employ an exponential time differencing (ETD) scheme.[57,58] The PSP approximation requires finding the saddle point of the μ_+ field for each configuration of $\{\mu'\}$. We use the ETD scheme for a fictitious time relaxation and terminate the search when the L_2 norm of the force falls below a tolerance of 10^{-6}.[56] A second-order Strang operator splitting algorithm is applied to solve Eq. (4) with a contour discretization of $\Delta s = 0.01$.[59,60] We choose the lattice discretization Δx to be equal to the statistical segment length b, corresponding to the conventional lattice cutoff used to regularize FTS methods. Here, $N = 100$ represents the number of numerical steps with step length $\Delta s = 1$ along the chain contour.[56,61] Here, $N = 100$ represents the number of numerical steps along the chain contour. In all cases studied here, $\zeta N = 100$. For reference calculations using DSCFT, we employ previously published semi-implicit schemes for time stepping the $\{\phi\}$ density fields and numerically computing the PSP auxiliary species fields $\{\psi\}$ at each time step.[62–64] The force tolerance for the PSP evaluation in DSCFT is set to an L_2 norm below 10^{-4}. All other shared parameters between EPD and DSCFT are kept consistent. An aggregate instantaneous structure factor is computed from

$$S(k,t) = \sum_{i,j=1}^{S} S_{ij}(k,t) - \sum_{i} S_{ii}(k,t) \tag{18}$$

with the component structure factors defined as

$$S_{ij}(k,t) = \langle \hat{\phi}_i(\mathbf{k},t)\hat{\phi}_j(-\mathbf{k},t)\rangle \tag{19}$$

where $\hat{\phi}_i(\mathbf{k},t)$ is the Fourier transform of the instantaneous density field (or density field operator).

Previous studies have shown that the variable transformation adopted in EPD can produce unphysical dynamical trajectories for strongly inhomogeneous systems with sharp spatial gradients. We have therefore restricted our EPD studies and DSCFT comparisons to coarsening simulations initialized from weakly inhomogeneous initial conditions.[34]

III. RESULTS

To validate the multi-component external potential dynamics (EPD) scheme, we compare the structural evolution during the formation of lamellae in an ABC triblock copolymer melt, starting from a homogeneous state perturbed by weak spatial noise. The triblock composition is

$\phi_A = \phi_C = 0.33$ and $\phi_B = 0.34$, with interaction parameters $\chi_{AB} = \chi_{BC} = 10.0$ and $\chi_{AC} = 20.0$. For the parameter set considered here we expect lamellae with alternating layers of all three components. In this case, thermal noise effects are neglected and based on the lamellar morphology, we only consider spatial variation only in one dimension (1D). The simulation box size was set equal to the lamellar domain period (determined through equilibrium SCFT calculations) and both the EPD and reference DSCFT simulations share the same initial conditions. Figure 1(a) shows the time-dependent growth of the maximum density of component A, a measure of the extent of microphase separation. While both EPD and DSCFT simulations exhibit similar overall trends, their trajectories differ quantitatively. EPD forms ordered domains sooner than DSCFT ($t/\tau \approx 1$), but both methods approach the equilibrium configuration at later times. To better illustrate the dynamics, we present two density profiles: one at $t/\tau \approx 0.7$, where the differences between the methods are most pronounced, and one at $t/\tau \approx 10$. Figure 1(b) highlights the early-stage coarsening at $t/\tau \approx 0.7$, where EPD shows significant departure from the homogeneous state, while DSCFT is just beginning to coarsen. By $t/\tau \approx 10$, shown in Figure 1(c), both methods have converged to similar equilibrium configurations. Although not quantitatively identical, the overall qualitative behavior of both methods is the same.

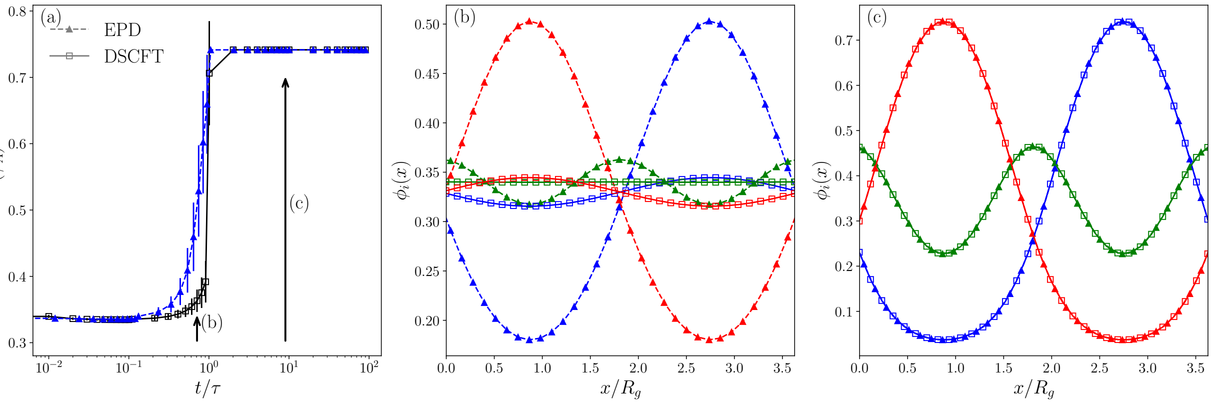

FIG. 1: Time-dependent growth of the amplitude in volume fraction of component A in an ABC triblock copolymer melt studied with both EPD and DSCFT simulations (1D). (a) Time evolution of the maximum volume fraction, showing faster coarsening for EPD near $t/\tau \approx 1$, while both methods converge at equilibrium. (b) Density profiles at $t/\tau \approx 0.7$ (red: A, blue: C, green: B), where EPD shows advanced coarsening. (c) Final equilibrium state at $t/\tau \approx 10$, where both methods produce similar results. The characteristic time τ is given by $\tau = R_g^2 C / D_{\text{Rouse}}$.

In previous work on two-species systems, EPD demonstrated quantitative agreement with

DSCFT methods that used non-local mobilities.[34] In contrast, the EPD scheme in this work coarsens similarly to a local mobility DSCFT approach. To understand the discrepancy, we remind the reader that EPD is normally based on a non-local Jacobian that utilizes a weak-amplitude expansion of the conventional density operator.[45] Here we use a local Jacobian based on the alternative density operator. Neither approach is without approximation, and there is no well-accepted methodology for constructing the Jacobian and modeling the mobility tensor. Fortunately, however, these differences in modeling approach do not seem to have significant impact on the qualitative dynamical behavior.

To continue our analysis, we next turn to a classic example: spinodal decomposition in a binary polymer blend.[65–68] Here, the polymers are symmetric both in architecture ($N_A = N_B = N$) and composition ($\bar{\phi}_A = \bar{\phi}_B = 0.5$), with an interaction parameter $\chi_{AB} = 4.0$. Unlike the previous example, we now account for thermal noise effects by including the final term in Eq. (14). Such an approach will be referred to as stochastic EPD (S-EPD). For visual clarity, the DSCFT, EPD, and S-EPD simulations are performed in a two-dimensional (2D) domain of size $125\ R_g \times 125\ R_g$. Figure 2 shows density distributions at different times during spinodal decomposition for DSCFT, EPD, and S-EPD. EPD and DSCFT display qualitatively similar patterns, though the DSCFT domains are generally smaller due to slower coarsening. The final row of the figure includes results from S-EPD ($C = 10.0$), which incorporates thermal fluctuations. In the early stages ($t/\tau = 1$), S-EPD shows significant differences from the deterministic EPD and DSCFT simulations, with small but well-defined phase-separated domains driven by thermal noise. At later stages, thermal fluctuations contribute minimally, resulting in rougher S-EPD interfaces but similar average domain sizes across simulation methods.

Analyzing the domain size provides a quantitative means to compare the structural evolution and coarsening behavior of EPD, DSCFT, and S-EPD. A measure of the domain size, $D(t)$, is provided by the first moment of the Fourier wavevector by $D(t) = \frac{2\pi}{\langle k(t) \rangle}$, where the instantaneous structure factor $S(k,t)$ is used to calculate $\langle k(t) \rangle$. This is expressed as $\langle k(t) \rangle = \frac{\int dk\, k\, S(k,t)}{\int dk\, S(k,t)}$. This definition accounts for the full spectrum of contributing wavevectors rather than relying solely on the dominant mode, making it a robust measure of domain size. Such an approach is particularly useful in stochastic simulations, where thermal fluctuations create significant roughness in $S(k)$, making it difficult to identify the dominant mode. Figure 3 displays averages with error bars derived from five replicates for each method or chain concentration.

Figure 3 (top) illustrates the time evolution of domain coarsening. Both the EPD model and

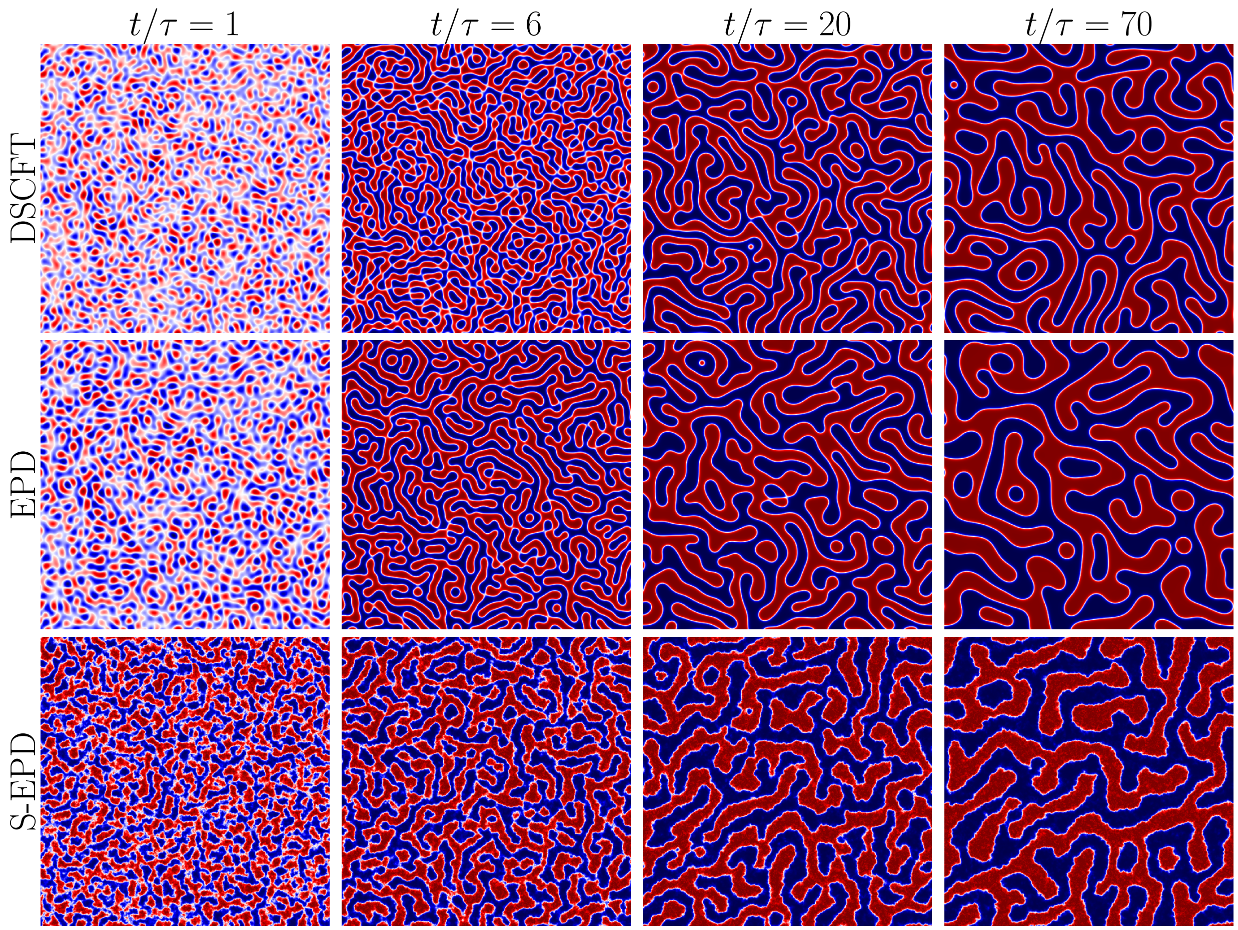

FIG. 2: Spinodal decomposition density patterns (A-species density) for a symmetric blend of A and B polymers at various times for DSCFT, EPD, and S-EPD ($C = 10.0$) in a 2D simulation box of size 125 $R_g \times 125$ R_g. The EPD and DSCFT simulations show qualitatively similar patterns, with DSCFT lagging slightly in coarsening. S-EPD demonstrates enhanced early-stage phase separation due to thermal fluctuations accelerating the growth of unstable modes and leading to rougher but similarly sized domains in later stages. Time (t) is rescaled in terms of τ, where τ is defined as $\tau = R_g^2 C/D_{\text{Rouse}}$.

the DSCFT model developed here exhibit domain growth that qualitatively follows the $1/3$ power law, as predicted by Ostwald ripening, which is confirmed by calculating the slope of the domain size growth curve.[69] However, quantitatively, DSCFT initially exhibits slower domain growth dynamics than EPD, resulting in slightly smaller domains. Figure 3 (bottom) presents the domain size over time for various chain concentrations C, where decreasing C amplifies fluctuations. The figure shows that fluctuations significantly impact early-stage domain growth ($t/\tau \sim 1$), while

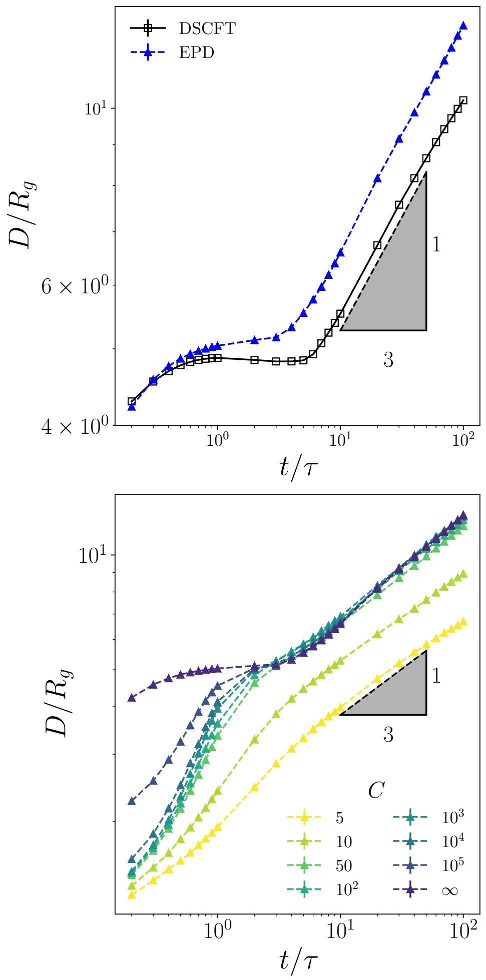

FIG. 3: Domain size evolution during spinodal decomposition of a binary symmetric polymer blend. (Top) Time series of domain growth comparison of EPD and DSCFT. The power law behavior (Oswald ripening) with exponent $1/3$ is followed by both methods. (Bottom) Time series of domain growth for the S-EPD method at different chain concentrations. Chain concentration is seen to most affect the early time coarsening rate, with the long time rate tracking deterministic power law behavior.

later-stage growth follows a more deterministic $1/3$ power law behavior. Additionally, increasing fluctuation strength tends to reduce domain size. These results suggest that as fluctuation strength increases, domain growth slows due to thermal effects, yet all simulations ultimately adhere to the $1/3$ power law characteristic of Ostwald ripening.

In Figure 2, the stochastic EPD domains at $\tau \sim 1$ appear more ordered compared to the deterministic simulations. This observation is supported by the plateau in domain growth seen in the deterministic simulations, as shown in Figure 3, in contrast to the smoother growth in the stochastic simulations. To quantify this ordering, we define the order parameter $\Omega(t) = \frac{S(k^*,t)}{1+S(k^*,t)}$, where k^* is the principal wavevector. Figure 4(a) shows the time series of the order parameter $\Omega(t)$

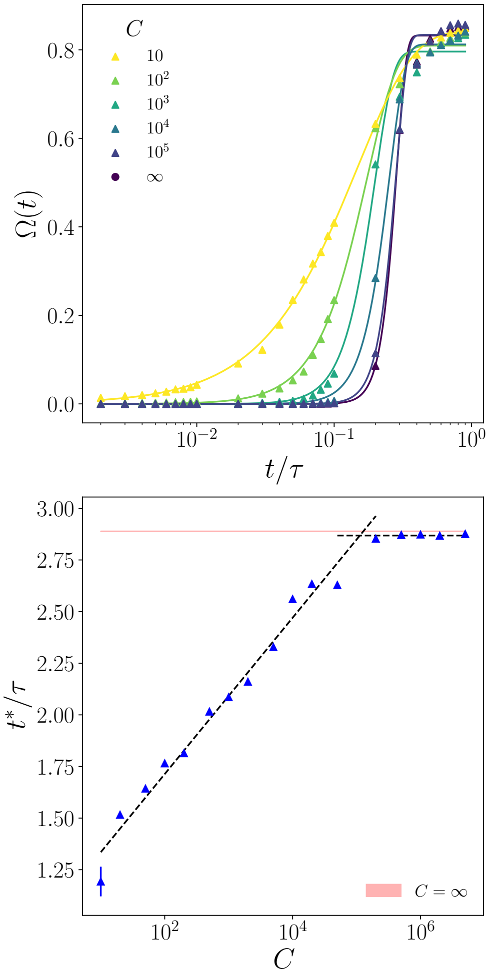

FIG. 4: The time dependence of the order parameter $\Omega(t)$ for various chain concentrations C in spinodal decomposition of a binary symmetric blend. (top) Time evolution of the order parameter, with fluctuations of increased strength inducing faster ordering at lower concentrations. (bottom) Critical coarsening time t^*/τ as a function of chain concentration, showing a crossover at approximately $C \sim 10^5$.

across different concentrations. The deterministic simulations ($C = \infty$) provide an upper limit on the ordering time, while decreasing C systematically shifts the ordering time earlier. All curves were fit to a stretched exponential of the form $f(t) = 1 - \exp\left(-(t/t^*)^\beta\right)$, where t^* is the critical coarsening time. Figure 4(b) shows the critical coarsening time t^*/τ as a function of chain concentration C. In the log-linear plot, two distinct regimes are evident: one where fluctuations induce earlier ordering, and another where fluctuations become sufficiently suppressed when approaching the $C = \infty$ limit. The crossover occurs at a relatively high chain concentration, around $C = 10^5$, indicating that all spinodal decomposition dynamics may be impacted by thermal fluctuations.

Next, we consider a ternary blend composed of architecturally symmetric chains with equal Flory-Huggins interaction parameters. Ternary mixtures are known for exhibiting a much richer phase behavior than two-component systems.[70] Although spinodal decomposition in ternary systems can proceed in different ways, the domains ultimately coarsen following the Ostwald ripening power-law of $1/3$.[71] Recent phase field simulation studies have identified four different phase separation pathways in ternary systems.[72]

Type I involves the simultaneous separation of all three components, forming a lattice-like morphology with distinct domains of each component interspersed.[72] Types II and III follow a two-stage separation process: Type II results in a worm-like morphology as consecutive pairs of components separate, while Type III produces a patchy droplet morphology where the third component enriches at interfaces and eventually forms droplets. Type IV resembles binary phase separation, where the minority component concentrates at the interfaces between the dominant phases.

To demonstrate the capabilities of EPD, we sweep the isopleth $\bar{\phi}_A$ (where $\bar{\phi}_B = \bar{\phi}_C = (1-\bar{\phi}_A)/2$) using $\chi_{AB}N = 10.0$ (where $\chi_{AB}N = \chi_{BC}N = \chi_{AC}N$) and report the resulting morphologies for Types I, II, and III. We find that DSCFT is highly inefficient in this regime, as solving for the saddle-point of the auxiliary fields at each time step requires more than 10^3 iterations. Therefore, we do not provide reference DSCFT simulation results. The EPD and S-EPD simulations are performed in a 2D domain with a box size of 125 $R_g \times 125$ R_g. Figure 5 shows configurations at two different coarsening times at three different compositions of ϕ_A: 0.33, 0.5, and 0.05. At $\bar{\phi}_A = 0.33$ we find Type I phase separation where a lattice morphology is formed with all three components interspersed. At $\bar{\phi}_A = 0.5$, a Type II morphology is observed comprising a worm-like structure built from two of the components. Finally, at $\bar{\phi}_A = 0.05$ we observe Type III structures, where binary spinodal decomposition is initiated, followed by enrichment of the third species at the interface.

We applied the prior domain size analysis to the coarsening data obtained at the three compositions to provide insight on the differences between the three types of phase separation and to confirm the coarsening mechanism. Additional simulations were conducted at $\bar{\phi}_A = 0.33$ to

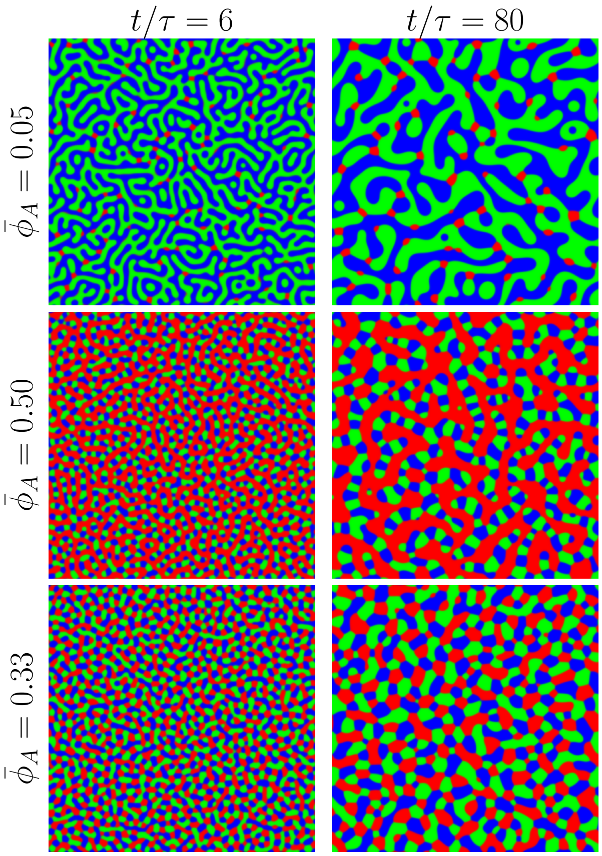

FIG. 5: Phase separation in ternary blends along the isopleth $\bar{\phi}_A$ (where $\bar{\phi}_B = \bar{\phi}_C = (1-\bar{\phi}_A)/2$) for various compositions of $\bar{\phi}_A$ at $t/\tau = 6$ and $t/\tau = 80$. (Middle) Type I morphology ($\bar{\phi}_A = 0.33$), showing interspersed domains of all components. (Bottom) Type II morphology ($\bar{\phi}_A = 0.50$), with worm-like domains. (Top) Type III morphology ($\phi_A = 0.05$), where binary spinodal decomposition is followed by enrichment of the third component at the interface. The 2D simulation domain is of size 125 $R_g \times 125$ R_g.

compare deterministic EPD simulations ($C = \infty$) with S-EPD conducted with a weak fluctuation strength ($C = 100$). Figure 6 (top) shows the characteristic size of domains as a function of time in EPD simulations of spinodally decomposing ternary blends. The three modes of phase separation differ the most at early times. The case of $\bar{\phi}_A = 0.05$ (Type III) appears to have similar phase separation behavior as the binary-polymer case. Namely, before $t/\tau \approx 1$ there is limited coarsening behavior, while thereafter coarsening proceeds with power law scaling and an exponent close to $\gamma = 1/3$. In contrast, both $\bar{\phi}_A = 0.33$ (Type I) and $\bar{\phi}_A = 0.5$ (Type II) systems exhibit domain contraction at early stages followed by power law coarsening beyond $t/\tau \approx 1$ with the same $1/3$ exponent. Curiously, the domain shrinkage behavior disappears when thermal fluctuations are

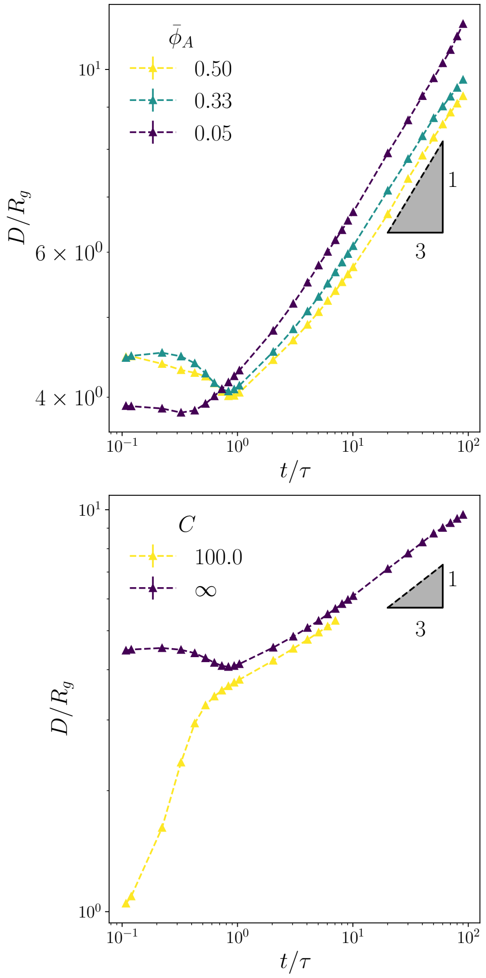

FIG. 6: Domain size coarsening analysis based on EPD simulations of different ternary blend compositions. (Top) Time series of domain sizes for $\bar{\phi}_A = 0.05$, $\bar{\phi}_A = 0.33$, and $\bar{\phi}_A = 0.50$, showing distinct early-stage coarsening behaviors. (Bottom) S-EPD simulations at $\bar{\phi}_A = 0.33$ demonstrate accelerated early stages of coarsening when weak thermal fluctuations ($C = 100$) are included.

included. Figure 6 (bottom) shows that S-EPD predicts smooth domain coarsening even before $t/\tau < 1$, indicating that fluctuations are essential to predicting early stage spinodal morphologies in frustrated blend systems.

Finally, Figure 7 presents a 3D simulation snapshots for two cases in a cubic domain with side length 32 R_g. The first case (Type II) has an average composition of $\bar{\phi}_A = 0.5$, while the second case (Type III) has $\bar{\phi}_A = 0.05$. Each snapshot captures a single configuration from the simulation trajectory at $t/\tau = 20$.

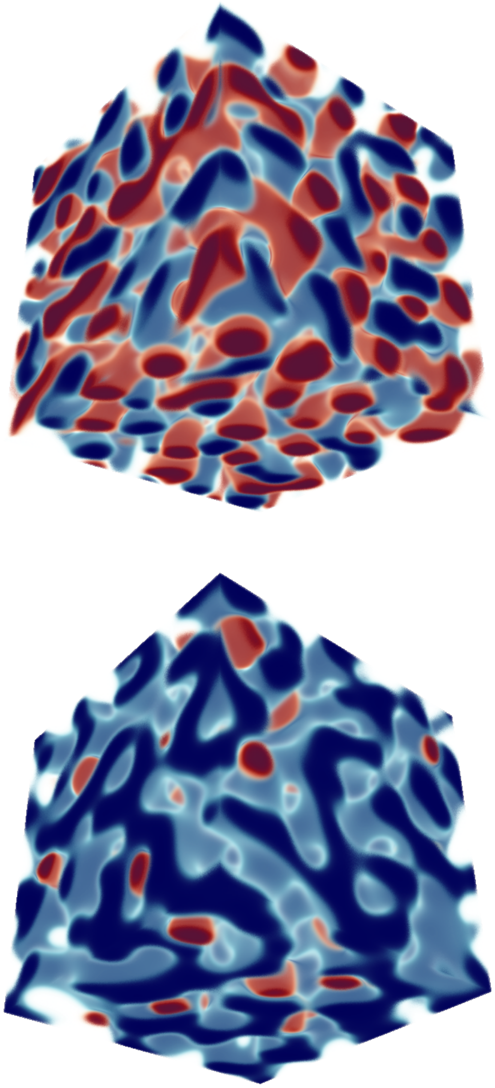

FIG. 7: 3D simulation snapshots for Type II ($\bar{\phi}_A = 0.50$) and Type III ($\bar{\phi}_A = 0.05$) ternary phase separations at $t/\tau = 20$ demonstrating the scalability of the methods to high-dimensional problems.

These results demonstrate that the EPD and S-EPD methods used here scale effectively to high-dimensional problems and can be applied to investigate the phase separation and coarsening behavior for a wide variety of complex polymer formulations.

IV. CONCLUSION

This paper presents the first external potential dynamics scheme that is generalized to include multi-species and multi-components with full thermal fluctuations. We demonstrate that the method produces qualitatively similar results to DSCFT, while being more computationally efficient and tolerant of thermal noise. In application to a binary polymer blend, the new stochastic EPD framework (S-EPD) was used to investigate the impact of thermal noise strength (controlled by the chain concentration C) on coarsening behavior in spinodal decomposition. While thermal agitation does not disrupt the classical 1/3 power law scaling of domain size expected at intermediate to long times, it strongly impacts the initial rate of domain size growth. We also showcased the ability of our new variant of EPD to study multi-component spinodal decomposition of a ternary polymer blend in both 2D and 3D simulations.

The present development of multi-species, multi-component EPD and S-EPD schemes open up interesting research opportunities that could immediately be pursued. For example, recent work on modeling the non-solvent-induced phase separation (NIPS) process used to manufacture asymmetric polymer membranes utilized stochastic phase field methods that are numerically unstable at realistic thermal noise strengths. Promising results were obtained by drastically scaling down the noise amplitude, but it is unclear how dynamical trajectories would change with thermodynamically consistent noise whose amplitude is set by the fluctuation-dissipation relation.[73,74] Another interesting area of investigation is to explore the role of surfactants or copolymer additives on the dynamics of non-equilibrium processes such as spinodal decomposition and nucleation and growth.[75,76] Such additives are known to dramatically slow phase separation and coarsening processes, or at high enough concentration, to arrest or completely change the kinetic pathway to the thermodynamically stable structure. This is an area ripe for investigation, but heretofore was awaiting computationally efficient multi-species, multi-component tools with realistic thermodynamic forces, diffusive dynamics, and thermal noise.

It is perhaps helpful to the reader to place our new S-EPD technique in a broader context. Apart from the partial saddle point (PSP) approximation that is used to deterministically relax the pressure mode, S-EPD can be viewed as a type of “field-theoretic simulation” (FTS) in that it embeds fully fluctuating thermodynamics.[20,23,77] Indeed, the variant of FTS practiced by the Matsen group for studying fluctuation effects in AB copolymer systems at equilibrium invokes the same PSP approximation on the pressure mode to improve stability and eliminate a sign problem. While the *fictitious* real Langevin dynamics practiced by that group, L-FTS, or the complex Langevin dynamics employed extensively by us, CL-FTS, are merely artifices to accumulate data on *equilibrium* states, the present S-EPD reflects a departure in two important directions. Firstly, it generalizes both approaches to address the *non-equilibrium* properties of polymer systems following mass-conserving, thermally agitated, multi-species diffusion. Secondly, it represents an extension of previous two-component EPD schemes to treat the non-equilibrium behavior of multi-species, multi-component polymer systems with full-strength thermal fluctuations. Overall, we are hopeful that the framework presented here will enable a deeper understanding of the non-equilibrium properties of broad classes of multi-component polymeric fluids.

ACKNOWLEDGMENTS

The authors thank Professor Hector Ceniceros, Dr. Duyu Chen, and Dr. Anthony Cooper for stimulating discussions. T. Q. was supported by the Center for Materials for Water and Energy Systems (M-WET), an Energy Frontier Research Center funded by the U.S. Department of Energy, Office of Science, Basic Energy Sciences under Award #DE-SC0019272. T.Q. gratefully acknowledge the NSF Graduate Research Fellowship Program (GRFP) under grant no. 2139319. C. B. was supported by the National Science Foundation under CMMT program award DMR-2104255. Use was made of computational facilities purchased with funds from the National Science Foundation (OAC-1925717) and administered by the Center for Scientific Computing (CSC). The CSC is supported by the California NanoSystems Institute and the Materials Research Science and Engineering Center (MRSEC; NSF DMR 2308708) at UC Santa Barbara.

DATA AVAILABILITY STATEMENT

The data that supports the findings of this study are available within the article and its supplementary material.

SUPPLEMENTARY MATERIAL

The supplementary material includes the derivation of the Jacobian for the change of variables, details on the noise generation algorithm and its validation, and additional numerical results. Videos of the results shown in the main text are also included.

REFERENCES

[1]I. R. Schmolka, Journal of the American Oil Chemists' Society **54**, 110 (1977), _eprint: https://onlinelibrary.wiley.com/doi/pdf/10.1007/BF02894385.

[2]A. George, P. A. Shah, and P. S. Shrivastav, International Journal of Pharmaceutics **561**, 244 (2019).

[3]P. Raffa, D. A. Z. Wever, F. Picchioni, and A. A. Broekhuis, Chemical Reviews **115**, 8504 (2015), publisher: American Chemical Society.

[4]C. Heinzmann, C. Weder, and L. M. d. Espinosa, Chemical Society Reviews **45**, 342 (2016), publisher: Royal Society of Chemistry.

[5]R. A. Shanks and I. Kong, in *Advances in Elastomers I: Blends and Interpenetrating Networks*, edited by P. M. Visakh, S. Thomas, A. K. Chandra, and A. P. Mathew (Springer, 2013) pp. 11–45.

[6]F. S. Bates, G. D. Wignall, and S. B. Dierker, Macromolecules **19**, 1938 (1986).

[7]J. M. Eagan, J. Xu, R. Di Girolamo, C. M. Thurber, C. W. Macosko, A. M. LaPointe, F. S. Bates, and G. W. Coates, Science **355**, 814 (2017), publisher: American Association for the Advancement of Science.

[8]J. Xu, J. M. Eagan, S.-S. Kim, S. Pan, B. Lee, K. Klimovica, K. Jin, T.-W. Lin, M. J. Howard, C. J. Ellison, A. M. LaPointe, G. W. Coates, and F. S. Bates, Macromolecules **51**, 8585 (2018), publisher: American Chemical Society.

[9]S. Velankar and S. L. Cooper, Macromolecules **33**, 382 (2000), publisher: American Chemical Society.

[10]S. Velankar and S. L. Cooper, Macromolecules **31**, 9181 (1998), publisher: American Chemical Society.

[11]M. Gradzielski, Current Opinion in Colloid & Interface Science **63**, 101662 (2023).

[12]V. Abetz, Macromolecular Rapid Communications **36**, 10 (2015), _eprint: https://onlinelibrary.wiley.com/doi/pdf/10.1002/marc.201400556.

[13]C.-y. Yang, G.-d. Zhu, Z. Yi, Y. Zhou, and C.-j. Gao, Chemical Engineering Journal **424**, 128912 (2021).

[14]N. Blagojevic and M. Müller, ACS Applied Materials & Interfaces **15**, 57913 (2023), publisher: American Chemical Society.

[15] G. H. Fredrickson, S. Xie, J. Edmund, M. L. Le, D. Sun, D. J. Grzetic, D. L. Vigil, K. T. Delaney, M. L. Chabinyc, and R. A. Segalman, ACS Polymers Au **2**, 299 (2022), publisher: American Chemical Society.

[16] J. Lequieu, T. Quah, K. T. Delaney, and G. H. Fredrickson, ACS Macro Letters **9**, 1074 (2020), publisher: American Chemical Society.

[17] J. A. Dolan, B. D. Wilts, S. Vignolini, J. J. Baumberg, U. Steiner, and T. D. Wilkinson, Advanced Optical Materials **3**, 12 (2015), _eprint: https://onlinelibrary.wiley.com/doi/pdf/10.1002/adom.201400333.

[18] F. S. Bates, M. A. Hillmyer, T. P. Lodge, C. M. Bates, K. T. Delaney, and G. H. Fredrickson, Science **336**, 434 (2012).

[19] T. E. I. Gartner and A. Jayaraman, Macromolecules **52**, 755 (2019), publisher: American Chemical Society.

[20] G. Fredrickson, *The Equilibrium Theory of Inhomogeneous Polymers* (Oxford University Press, 2005) https://doi.org/10.1093/acprof:oso/9780198567295.001.0001.

[21] F. Schmid, ACS Polym. Au **3**, 28 (2023), publisher: American Chemical Society.

[22] T. E. I. Gartner and A. Jayaraman, Macromolecules **52**, 755 (2019), publisher: American Chemical Society.

[23] G. H. Fredrickson and K. T. Delaney, *Field-Theoretic Simulations in Soft Matter and Quantum Fluids* (Oxford University Press, 2023) https://academic.oup.com/book/45705/book-pdf/50133196/9780192663238_web.pdf.

[24] F. Schmid, Journal of Physics: Condensed Matter **10**, 8105 (1998), https://dx.doi.org/10.1088/0953-8984/10/37/002.

[25] M. W. Matsen, Journal of Physics: Condensed Matter **14**, R21 (2001), https://dx.doi.org/10.1088/0953-8984/14/2/201.

[26] M. W. Matsen, Soft Matter **1** (2006).

[27] A. Arora, J. Qin, D. C. Morse, K. T. Delaney, G. H. Fredrickson, F. S. Bates, and K. D. Dorfman, Macromolecules **49**, 4675 (2016), https://doi.org/10.1021/acs.macromol.6b00107.

[28] M. Müller and F. Schmid (Springer, Berlin, Heidelberg, 2005) pp. 1–58.

[29] J. G. E. M. Fraaije, The Journal of Chemical Physics **99**, 9202 (1993).

[30] J. G. E. M. Fraaije, B. A. C. van Vlimmeren, N. M. Maurits, M. Postma, O. A. Evers, C. Hoffmann, P. Altevogt, and G. Goldbeck-Wood, The Journal of Chemical Physics **106**, 4260 (1997).

[31] C. Yeung and A.-C. Shi, Macromolecules **32**, 3637 (1999), publisher: American Chemical Society.

[32] R. Hasegawa and M. Doi, Macromolecules **30**, 3086 (1997), publisher: American Chemical Society.

[33] P. C. Hohenberg and B. I. Halperin, Reviews of Modern Physics **49**, 435 (1977), publisher: American Physical Society.

[34] S. Qi and F. Schmid, Macromolecules **50**, 9831 (2017), publisher: American Chemical Society.

[35] G. J. A. Sevink and A. V. Zvelindovsky, Macromolecules **38**, 7502 (2005), publisher: American Chemical Society.

[36] S. P. Paradiso, K. T. Delaney, C. J. García-Cervera, H. D. Ceniceros, and G. H. Fredrickson, Macromolecules **49**, 1743 (2016), publisher: American Chemical Society.

[37] S. P. Paradiso, K. T. Delaney, C. J. García-Cervera, H. D. Ceniceros, and G. H. Fredrickson, ACS Macro Letters **3**, 16 (2014), publisher: American Chemical Society.

[38] X. Li, P. Tang, H. Zhang, F. Qiu, and Y. Yang, The Journal of Chemical Physics **128**, 114901 (2008).

[39] D. M. Hall, T. Lookman, G. H. Fredrickson, and S. Banerjee, Physical Review Letters **97**, 114501 (2006).

[40] T. Honda and T. Kawakatsu, The Journal of Chemical Physics **129**, 114904 (2008).

[41] B. A. C. van Vlimmeren and J. G. E. M. Fraaije, Computer Physics Communications **99**, 21 (1996).

[42] T. Quah, K. T. Delaney, and G. H. Fredrickson, The Journal of Chemical Physics **161**, 244104 (2024), https://pubs.aip.org/aip/jcp/article-pdf/doi/10.1063/5.0241609/20314819/244104_1_5.0241609.pdf.

[43] E. Reister, M. Müller, and K. Binder, Physical Review E **64**, 041804 (2001), publisher: American Physical Society.

[44] X. He and F. Schmid, Macromolecules **39**, 2654 (2006), publisher: American Chemical Society.

[45] N. M. Maurits and J. G. E. M. Fraaije, The Journal of Chemical Physics **107**, 5879 (1997).

[46] S. Qi, X. Zhang, and D. Yan, The Journal of Chemical Physics **132**, 064903 (2010).

[47] E. Reister and M. Müller, The Journal of Chemical Physics **118**, 8476 (2003).

[48] W. Li and W. Jiang, e-Polymers **10** (2010), 10.1515/epoly.2010.10.1.597, publisher: De Gruyter.

[49] X. He and F. Schmid, Phys. Rev. Lett. **100**, 137802 (2008).

[50] V. Raman, T. A. Hatton, and B. D. Olsen, Macromolecular Rapid Communications **35**, 2005 (2014), _eprint: https://onlinelibrary.wiley.com/doi/pdf/10.1002/marc.201400373.

[51] J. J. Fan, W. Li, Z. D. Pan, and M. F. Shi, Advanced Materials Research **915-916**, 545 (2014), publisher: Trans Tech Publications Ltd.

[52] J. Heuser, G. J. A. Sevink, and F. Schmid, Macromolecules **50**, 4474 (2017), publisher: American Chemical Society.

[53] D. Düchs, K. T. Delaney, and G. H. Fredrickson, The Journal of Chemical Physics **141**, 174103 (2014), https://doi.org/10.1063/1.4900574.

[54] E. Helfand, The Journal of Chemical Physics **62**, 999 (1975), https://doi.org/10.1063/1.430517.

[55] K. T. Delaney and G. H. Fredrickson, The Journal of Physical Chemistry B **120**, 7615 (2016), pMID: 27414265, https://doi.org/10.1021/acs.jpcb.6b05704.

[56] B. Vorselaars, P. Stasiak, and M. W. Matsen, Macromolecules **48**, 9071 (2015), https://doi.org/10.1021/acs.macromol.5b02286.

[57] S. Cox and P. Matthews, J. Comput. Phys. **176**, 430 (2002), http://www.sciencedirect.com/science/article/pii/S0021999102969950.

[58] M. C. Villet and G. H. Fredrickson, The Journal of Chemical Physics **132**, 034109 (2010), https://pubs.aip.org/aip/jcp/article-pdf/doi/10.1063/1.3289723/15669136/034109_1_online.pdf.

[59] K. Ø. Rasmussen and G. Kalosakas, J. Polym. Sci., Part B: Polym. Phys. **40**, 1777 (2002), https://onlinelibrary.wiley.com/doi/pdf/10.1002/polb.10238.

[60] G. Tzeremes, K. Ø. Rasmussen, T. Lookman, and A. Saxena, Phys. Rev. E **65**, 041806 (2002), https://link.aps.org/doi/10.1103/PhysRevE.65.041806.

[61] T. M. Beardsley and M. W. Matsen, The Journal of Chemical Physics **150**, 174902 (2019), https://pubs.aip.org/aip/jcp/article-pdf/doi/10.1063/1.5089217/13777228/174902_1_online.pdf.

[62] D. J. Grzetic, A. J. Cooper, K. T. Delaney, and G. H. Fredrickson, ACS Macro Letters **12**, 8 (2023), publisher: American Chemical Society.

[63] H. D. Ceniceros and G. H. Fredrickson, Multiscale Modeling & Simulation **2**, 452 (2004), https://doi.org/10.1137/030601338.

[64] E. M. Lennon, G. O. Mohler, H. D. Ceniceros, C. J. García-Cervera, and G. H. Fredrickson, Multiscale Modeling & Simulation **6**, 1347 (2008), https://doi.org/10.1137/070689401.

[65] P. G. De Gennes, The Journal of Chemical Physics **72**, 4756 (1980).

[66] P. Pincus, The Journal of Chemical Physics **75**, 1996 (1981).

[67] G. R. Strobl, Macromolecules **18**, 558 (1985).

[68] K. Binder, C. Billotet, and P. Mirold, Zeitschrift für Physik B Condensed Matter **30**, 183 (1978).

[69] I. M. Lifshitz and V. V. Slyozov, Journal of Physics and Chemistry of Solids **19**, 35 (1961).

[70] E. B. Nauman and D. Q. He, Polymer **35**, 2243 (1994).

[71] C. Huang, M. O. de la Cruz, and B. W. Swift, Macromolecules **28**, 7996 (1995), publisher: American Chemical Society.

[72] A. C. M. Shek and H. Kusumaatmaja, Soft Matter **18**, 5807 (2022), publisher: Royal Society of Chemistry.

[73] J. U. Garcia, T. Iwama, E. Y. Chan, D. R. Tree, K. T. Delaney, and G. H. Fredrickson, ACS Macro Letters **9**, 1617 (2020), publisher: American Chemical Society.

[74] M. R. Cervellere, X. Qian, D. M. Ford, C. Carbrello, S. Giglia, and P. C. Millett, Journal of Membrane Science **619**, 118779 (2021).

[75] M. Takenaka and T. Hashimoto, Macromolecules **29**, 4134 (1996), publisher: American Chemical Society.

[76] T. Hashimoto and T. Izumitani, Macromolecules **26**, 3631 (1993).

[77] G. H. Fredrickson, V. Ganesan, and F. Drolet, Macromolecules **35**, 16 (2002), https://doi.org/10.1021/ma011515t.